JOURNAL OF GEOPHYSICAL RESEARCH, VOL. 106, NO. D19, PAGES 22,907–22,922, OCTOBER 16, 2001

Analysis of smoke impact on clouds in Brazilian biomass burning regions: An extension of Twomey's approach

Graham Feingold
NOAA Environmental Technology Laboratory, Boulder, Colorado, USA

Lorraine A. Remer, Jaya Ramaprasad, and Yoram J. Kaufman
NASA Goddard Space Flight Center, Greenbelt, Maryland, USA

Abstract. Satellite remote sensing of smoke aerosol-cloud interaction during the recent Smoke, Clouds, and Radiation–Brazil (SCAR–B) experiment is analyzed to explore the factors that determine the magnitude of the cloud response to smoke aerosol. Analysis of 2 years worth of data revealed that the response is greatest in the north of Brazil where aerosol optical depth is smallest, and tends to decrease as one moves southward, and as aerosol optical depth increases. Saturation in this response occurs at an aerosol optical depth of 0.8 in 1987 and 0.4 in 1995. To explore the reasons for this, a framework is developed in which the satellite-measured response can be compared to simple analytical models of this response and to numerical models of smoke aerosol-cloud interaction. Three types of response are identified: (1) cloud droplet concentrations increase with increasing aerosol loading, followed by saturation in the response at high concentrations; (2) as in type 1, followed by increasing droplet concentrations with further increases in aerosol loading. This increase in droplet concentration is due to the suppression of supersaturation by abundant large particles, which prevents the activation of smaller particles. This enables renewed activation of larger particles when smoke loadings exceed some threshold; (3) as in type 1, followed by a decrease in droplet number concentrations with increasing aerosol loading as intense competition for vapor evaporates the smaller droplets. The latter implies an unexpected increase in drop size with increasing smoke loading. The conditions under which each of these responses are expected to occur are discussed. It is shown that although to first-order smoke optical depth is a good proxy for aerosol indirect forcing, under some conditions the size distribution and hygroscopicity can be important factors. We find no evidence that indirect forcing depends on precipitable water vapor.

1. Introduction

In discussing aerosol, the term "indirect effect" has been coined to describe climatic implications for the interaction of solar radiation with aerosol particles that are hygroscopic and can participate as cloud condensation nuclei (CCN) [e.g., *Twomey*, 1974; *Charlson et al*., 1992]. Twomey hypothesized that increased concentrations of atmospheric aerosol will result in higher concentrations of CCN and increased cloud droplet concentrations. This chain of events will affect cloud microphysical processes. Higher droplet concentrations will suppress drizzle formation [*Albrecht*, 1989] and maintain larger liquid water paths and more reflective clouds. The more reflective clouds, in theory, create a radiative forcing estimated on the global scale to range from 0.0 W m^{-2} to -4.8 W m^{-2} [*Kaufman et al*., 1991; *Charlson et al*., 1992; *Kaufman and Chou*, 1993; *Lohmann and Feichter*, 1997]. One manifestation of these processes is in "ship tracks," the observed bright tracks in stratus clouds which are produced by the high aerosol concentrations in ship effluent [*Conover*, 1966; *Coakley et al*., 1987]. Ship track experiments have been valuable in elucidating the microphysical processes that create these more reflective clouds. (e.g., the Monterey Area Ship Track Experiment, 1994). Because the indirect effect is defined as a climatic forcing, it is necessary to evaluate it on a regional or global scale using satellite remote sensing. Such efforts have been undertaken in South American biomass burning regions by *Kaufman and Nakajima* [1993] and *Kaufman and Fraser* [1997] (hereinafter referred to as KF97), in Indonesian fires by *Rosenfeld and Lensky* [1998], and globally for all aerosol types collocated with marine stratus clouds by *Wetzel and Stowe* [1999]. These papers provide evidence in support of Twomey's theory beyond the limited environment of the ship track experiments. However, they also show variation in the strength of the indirect effect that cannot be explained by Twomey's simple formulation.

The indirect effect has also been observed by careful in situ measurements that link changes in cloud properties to changes in aerosol concentration or proxy [*Leaitch et al*., 1992; *Raga and Jonas*, 1993; *Novakov et al*., 1994; *Arends et al*., 1994; *Leaitch et al*., 1996; *Reid et al*., 1998]. These studies identify situations where the connection between aerosol and cloud microphysics is clear, while in other situations, no connection appears to exist. However, the conclusions differ widely. For example, some in situ studies identify the indirect effect in stratiform clouds but not in cumuliform clouds [*Novakov et al*., 1994; *Reid et al*., 1999]. Other studies clearly find the effect in cumuliform clouds [*Raga and Jonas*, 1993; *Arends et al*., 1994].

Paper number 2001JD000732.

These studies provide evidence supporting Twomey's original theory but leave us with unanswered questions. Why do we sometimes see the indirect effect and sometimes not? Is it due to variations in precipitable water vapor as hypothesized by KF97? Are the differences due to cloud type, dynamics, or turbulence, as hypothesized by *Novakov et al*. [1994], *Arends et al*. [1994], *Leaitch et al*. [1996], and *Reid et al*. [1999], or can the differences be explained by variations in the aerosol properties themselves? The observational studies alone have not been able to provide definitive answers.

In this paper we turn to a combination of satellite observations and theoretical modeling for the answers to these questions. The area of interest is the biomass burning region of South America, which provided the focus of the papers of *Kaufman and Nakajima* [1993] and KF97. The primary goals of this paper are to (1) develop a framework that facilitates the intercomparison of satellite measurements and models, (2) extend the analysis of KF97 to an additional year of data and to evaluate whether the conclusions and water vapor hypothesis of the first paper are robust under different data and newer precipitable water vapor analyses, and (3) explore the reasons for the observed variability in the indirect aerosol forcing using some simple theoretical and modeling exercises.

The remainder of this paper is organized as follows: in section 2 we consider the theoretical and semiempirical theories that form the basis of evaluation of aerosol indirect forcing; in section 3 we present new analysis of the 1987 and 1995 South American biomass burning data; and in section 4 we apply the theory and modeling framework to interpret the observations. We conclude with a summary in section 5.

2. Simple Analytical Models

KF97 derived a measure of the aerosol indirect effect as

$$\frac{\Delta r_e}{\Delta \tau_a}, \tag{1}$$

where r_e is the droplet effective radius (the ratio of the third and second moments of the drop size distribution), and τ_a is the smoke aerosol optical depth. To put those measurements in the perspective of prior studies, we propose the calculation of

$$\mathrm{IE} = -\frac{\tau_a}{r_e}\frac{\Delta r_e}{\Delta \tau_a} = -\frac{d \ln r_e}{d \ln \tau_a}, \tag{2}$$

which represents the relative change in r_e for a relative change in τ_a. IE refers to the "indirect effect" and is defined as positive in sign if an increase in τ_a results in a decrease in r_e. The attractive feature of assessing the cloud response to aerosol using (2) is that by considering relative changes in parameters, one is less susceptible to measurement errors than in the formulation of (1). The equation for cloud optical depth τ_d in the visible region of the spectrum is given by

$$\tau_d \approx \int_{z_b}^{z_t}\int_{r_{\min}}^{\infty} 2\pi r^2 n(r)\, dr\, dz, \tag{3}$$

where $n(r)$ defines the drop spectrum with respect to radius r, z_b is cloud base, z_t is cloud top, $r_{\min}$ is the minimum drop radius, and the extinction efficiency has been assumed to be equal to 2. (A similar equation defines aerosol optical depth τ_a but with $n(r)$ describing the aerosol size distribution and z_b and z_t the smoke layer boundaries; for aerosol the extinction efficiency should be explicitly calculated for the appropriate wavelength and particle composition.) For a homogeneous cloud with drop number concentration N_d and constant cloud liquid water content LWC, (3) reduces to

$$\tau_d \propto N_d^{1/3} \tag{4}$$

[*Twomey*, 1977]. Assuming that N_d obeys

$$N_d \propto N_a^{a_1}, \tag{5}$$

where N_a is the aerosol number concentration [*Twomey*, 1977], and using (4) and (5) yields

$$r_e \propto \tau_a^{-a_1/3}, \tag{6}$$

$$-\frac{d \ln r_e}{d \ln \tau_a} = \frac{a_1}{3}. \tag{7}$$

A characteristic value of a_1 is 0.7 [e.g., *Pruppacher and Klett*, 1997; *Charlson et al*., 1987], yielding IE = 0.23. Note that since $a_1 \leq 1$, we obtain $0 \leq \mathrm{IE} \leq 0.33$.

Equation (5) is clearly a simplification of the relationship between aerosol microphysics and cloud microphysics since cloud parameters and aerosol parameters are related through the aerosol size distribution parameters and updraft velocity, rather than just through N_a.

The analysis is now extended to include aerosol size parameters. Smoke aerosol size distributions vary but are often parameterized by a lognormal function [e.g., *Remer et al*., 1998] with respect to aerosol particle radius a:

$$n(a) = \frac{N_a}{\sqrt{2\pi}\ln \sigma a}\, e^{-\ln^2(a/r_g)/(2\ln^2\sigma)}, \tag{8}$$

where r_g is the median radius, and σ is the geometric standard deviation of the aerosol particles. We have varied N_a, r_g, and σ over a broad range of parameter space to represent possible biomass burning scenarios (Table 1):

$$0.04\ \mu\mathrm{m} \leq r_g \leq 0.12\ \mu\mathrm{m}; \qquad 2000\ \mathrm{cm}^{-3} \leq N_a \leq 30000\ \mathrm{cm}^{-3}; \qquad 1.3 \leq \sigma \leq 2.2. \tag{9}$$

We assume, for the sake of simplicity, that

$$\tau_a \propto N_a^{b_1} r_g^{b_2} \sigma^{b_3}, \tag{10}$$

$$N_d \propto N_a^{a_1}\, r_g^{a_2}\, \sigma^{a_3}\, w^{a_4}, \tag{11}$$

where w is the updraft velocity. The first approximation is justified by the good fit to accurate calculations of τ_a based on

Table 1. Lognormal Input Parameters and Updraft Velocities for the Model

N_a, cm^{-3}	r_g, μm	σ	w, cm s^{-1}
2000	0.04	1.3	20
4000	0.05	1.4	50
6000	0.06	1.5	75
8000	0.07	1.6	100
10000	0.08	1.7	150
12000	0.09	1.8	200
15000	0.10	2.0	300
20000	0.11	2.2	
25000	0.12		
30000			

Mie calculations for spherical aerosol particles at 0.64 μm (Figure 1). The values of b_1, b_2, and b_3 depend on the refractive index of the aerosol (assumed here to be $m = 1.6 + 0.1i$). For these conditions a least squares fit to the model output over the range of lognormal aerosol size distributions in (9) yields $b_1 = 1.0$ (as predicted by the definition of τ_a), $b_2 = 3.4$, and $b_3 = 5.0$.

To explore the second approximation (11), we use an entraining parcel model of cloud droplet formation [*Feingold and Heymsfield*, 1992]. The model rigorously calculates the uptake of water vapor by a size distribution of aerosol particles, their subsequent activation, and growth by condensation. It has the flexibility to modify the solubility of the particles and the extent of entrainment drying. Entrainment is simulated as a depletion of total water mixing ratio (vapor plus liquid water) with droplets growing or evaporating in response to the change in supersaturation. It is assumed that the smoke is not replenished by entrainment since the source of the smoke is primarily a surface source.

The dynamics of the model are prescribed by a constant updraft velocity w, so it does not represent the myriad microphysical, or radiative feedbacks to the dynamics, such as destabilization/stabilization of the atmosphere as a result of absorption, or feedbacks of the aerosol to cloud liquid water path (LWP). Although the model is a simplification of real clouds, it does provide a means of exploring the relative changes in response for different aerosol input, updraft velocity, and cloud depth, and should be viewed in this light, rather than as an accurate representation of the clouds observed during SCAR–B.

The smoke particles in SCAR–B are primarily organics [e.g., *Artaxo et al.*, 1998] with rather complex water uptake properties. They are quite different from sulfate particles in industrial regions and from the aerosol representation originally in the work of *Feingold and Heymsfield* [1992]. Therefore we have modified the aerosol treatment in the current work. Because no general models exist to represent the hygroscopic activity of organic particles, we have used nephelometer data collected during SCAR–B [*Kotchenruther and Hobbs*, 1998] as a means of constraining their water vapor uptake. The nephelometer data yield a relationship between the relative increase in the total light scattering coefficient as a function of relative humidity. The hygroscopicity of the modeled aerosol is attained by modifying the mass fraction of soluble material ε until the enhancement in scattering as a function of RH provides a reasonable fit to the observed data. Although this is a rather crude way of representing the growth properties of complex organic particles, it does provide a strong constraint on their uptake of water vapor and potential for growth into droplets.

As shown in Figure 2, (11) is a good approximation to the model output for the parameter space defined by (9) and provides a significantly better fit than more simple forms such as (5). The standard error of estimate is low, considering that N_d is typically 10^3 to 10^4. We offer no physical justification for the power law form, other than that it provides a logical extension to the original form proposed by *Twomey* [1959]

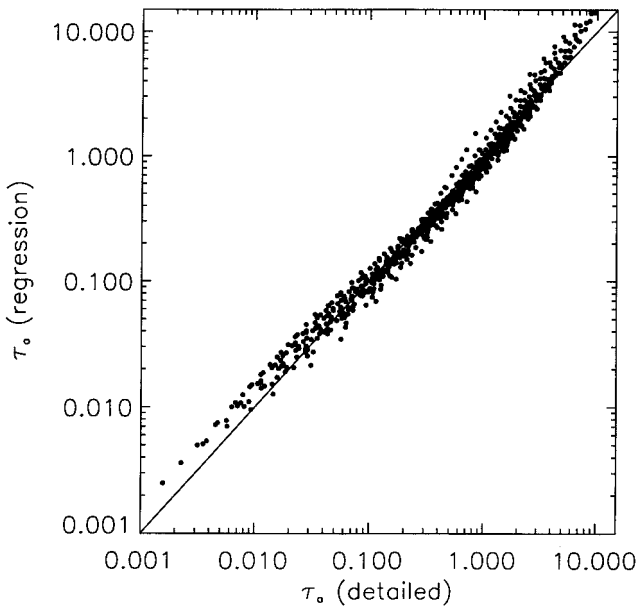

Figure 1. Comparison of two calculations of τ_a at 0.64 μm. The ordinate is based on detailed extinction calculations assuming a lognormal aerosol spectrum (Table 1) comprising spherical particles, a refractive index of $m = 1.6 + 0.1i$, and a homogeneous smoke depth of 1 km. The abscissa values of τ_a are based on the power law regression fit given by equation (10). The standard error of estimate for the regression fit is 0.86.

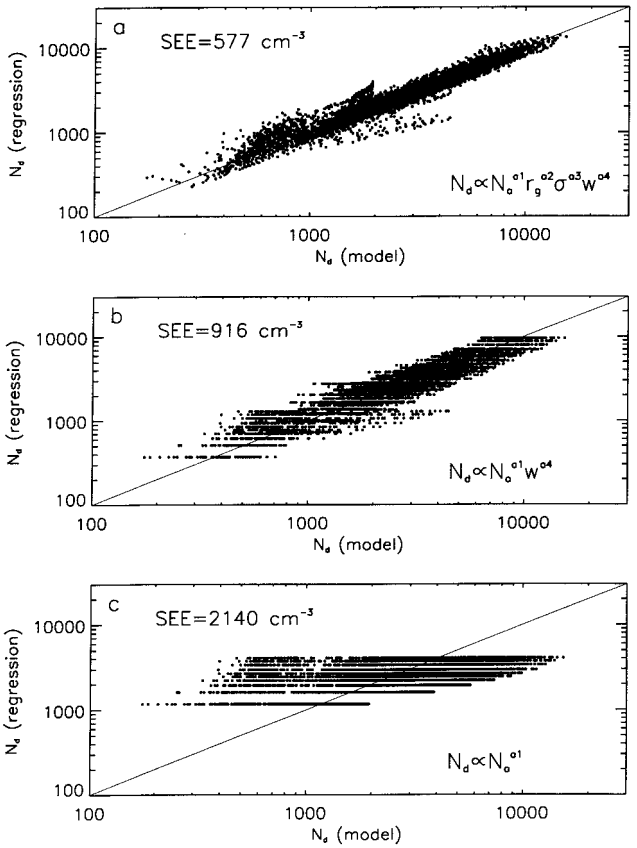

Figure 2. Comparison of parcel model calculations of N_d defined as all drops with $r \geq 1$ μm and N_d calculated using (a) the power law regression fit given by equation (11); (b) a two-parameter regression; and (c) a fit defined by equation (5). The results pertain to a LWP of 15 g m^{-2}, and $\varepsilon = 0.1$. All input parameters in Table 1 have been used to generate the regression. The standard error of estimate is indicated in each figure.

Table 2. Coefficients a_n for $N_d \propto N_a^{a_1} r_g^{a_2} \sigma^{a_3} w^a$[a]

Aerosol Parameters/Updraft	a_1	a_2	a_3	a_4	IE
$\varepsilon = 0.1$	0.46	0.52	−0.55	0.74	0.17
$\varepsilon = 0.1$ (half adiabatic)	0.41	0.87	0.37	0.77	0.24
$\varepsilon = 0.1$ (LWP = 50)	0.44	0.48	−0.50	0.76	0.16
$\varepsilon = 1.0$	0.38	0.04	−2.80	0.52	−0.06
$0.04 \le r_g \le 0.08$	0.53	0.29	−0.46	0.84	0.17
$0.08 \le r_g \le 0.12$	0.50	−0.10	−0.51	0.73	0.12
(equivalent τ_a)	0.56	0.33	−0.43	0.79	0.19
$N_a \le 5000$ cm^{-3}	0.77	0.50	−0.63	0.59	0.26
(equivalent τ_a)	0.56	0.38	−0.45	0.84	0.19
$N_a > 5000$ cm^{-3}	0.57	0.40	−0.42	0.82	0.20
$1.3 \le \sigma \le 1.6$	0.54	0.37	−0.35	0.87	0.19
$1.6 \le \sigma \le 2.2$	0.58	0.35	−0.06	0.73	0.22
$w \le 100$	0.53	0.42	0.06	0.88	0.22
$w \ge 200$	0.59	0.31	−0.82	0.77	0.17
$w \le 100$, $r_g \le 0.08$, $N_a \le 5000$	0.75	0.75	−0.33	0.77	0.30
(equivalent τ_a)	0.60	0.48	−0.31	0.83	0.22
$w \ge 200$, $r_g > 0.08$, $N_a > 5000$	0.49	−0.04	−1.13	0.84	0.08
(equivalent τ_a)	0.57	0.33	−0.41	0.79	0.19

[a]IE represents the indirect effect, as defined in equation (18). Coefficients are valid for LWP = 15 g m^{-2}, 0.04 μm $\le r_g \le$ 0.12 μm; 2000 cm$^{-3} \le N_a \le$ 30,000 cm^{-3}; $1.3 \le \sigma \le 2.2$; 20 cm s$^{-1} \le w \le$ 300 cm s^{-1}, $\varepsilon = 0.1$, and an adiabatic cloud, unless otherwise stated in column 1. Equivalent τ_a is defined as the range of τ_a prescribed by the aerosol parameters in the row directly preceding the table entry but with no constraints on the lognormal parameters.

$$N_d \propto C^{1-k/(k+2)} w^{1.5k/(k+2)}, \tag{12}$$

where C is related to N_a, and k is a parameter related to the slope of a power law size distribution of aerosol. An advantage of (11) is that the power law form facilitates the inclusion of aerosol size parameters into the subsequent analysis. The values of a_1, a_2, a_3, and, a_4 have been derived by running the model for the input parameters indicated in Table 1, for typical meteorological conditions for the region, and performing least fit multivariate regressions to the model output. Each regression is performed on a total of 5040 realizations of the model.

The drop concentration N_d represents all drops with $r \ge 1$ μm. It is recognized that at very high N_a, many particles may exist as unactivated haze particles [e.g., *Reid et al*., 1999], but the exact definition of the minimum droplet radius is not very important because as soon as the larger particles that have reached their critical size begin to grow, the smaller haze particles find themselves in increasingly subsaturated conditions and evaporate rapidly, thus effectively separating haze particles from drops.

The coefficients depend on aerosol water uptake and the range of N_a, r_g, σ, and w; the goodness of fit improves if the fit is done in piecewise fashion. Table 2 tabulates a_n for the parameter space in (9) and for a variety of conditions. Note that a_n do not vary with LWP. Discussion of the significance of these coefficients is deferred to section 4.

The analysis of smoke aerosol effect on clouds proceeds as follows:

$$\frac{dr_e}{d\tau_a} = \frac{dr_e}{dN_d}\frac{dN_d}{d\tau_a}. \tag{13}$$

At constant LWC,

$$\frac{dr_e}{dN_d} = -\frac{1}{3}\frac{r_e}{N_d}. \tag{14}$$

Then,

$$\frac{dN_d}{d\tau_a} = \frac{\partial N_d}{\partial N_a}\frac{dN_a}{d\tau_a} + \frac{\partial N_d}{\partial r_g}\frac{dr_g}{d\tau_a} + \frac{\partial N_d}{\partial \sigma}\frac{d\sigma}{d\tau_a}, \tag{15}$$

and using (10) and (11),

$$\frac{dN_d}{d\tau_a} = \frac{N_d}{\tau_a}\left[\frac{a_1}{b_1} + \frac{a_2}{b_2} + \frac{a_3}{b_3}\right]. \tag{16}$$

Finally,

$$\frac{dr_e}{d\tau_a} = \frac{dr_e}{dN_d}\frac{dN_d}{d\tau_a} = -\frac{1}{3}\frac{r_e}{N_d}\frac{N_d}{\tau_a}\left[\frac{a_1}{b_1} + \frac{a_2}{b_2} + \frac{a_3}{b_3}\right], \tag{17}$$

or

$$\mathrm{IE} = -\frac{d\ln r_e}{d\ln \tau_a} = \frac{1}{3}\left[\frac{a_1}{b_1} + \frac{a_2}{b_2} + \frac{a_3}{b_3}\right]. \tag{18}$$

Equation (18) reduces to (7) under the assumption of (5) and is thus a more general description of aerosol-cloud interaction, as defined by (2). According to (18) there are no clear bounds on the value of IE, as was the case with (7).

Because cloud reflectance and smoke optical depth are directly measured, rather than inferred, an additional parameter to explore is the relative change in cloud reflectance ρ for a relative change in τ_a:

$$\frac{d\ln \rho}{d\ln \tau_a} = \frac{d\ln \rho}{d\ln r_e}\frac{d\ln r_e}{d\ln \tau_a}, \tag{19}$$

Using the two-stream approximation for a purely scattering cloud [*Bohren*, 1980],

$$\rho \approx \frac{(1-g)\tau_d}{2 + (1-g)\tau_d}, \tag{20}$$

where g is the asymmetry factor ($\approx$0.85), as well as

$$\tau_d = \frac{3}{2}\frac{\mathrm{LWP}}{r_e} \tag{21}$$

[*Stephens*, 1978], we can differentiate (20) with respect to r_e to obtain

$$\frac{d \ln \rho}{d \ln r_e} = -(1-\rho). \tag{22}$$

Then substituting (18) and (22) into (19) yields

$$\frac{d \ln \rho}{d \ln \tau_a} = \frac{(1-\rho)}{3}\left[\frac{a_1}{b_1} + \frac{a_2}{b_2} + \frac{a_3}{b_3}\right] = (1-\rho)\mathrm{IE}. \tag{23}$$

Equation (23) provides an alternative meaning of IE and an alternative means of acquiring a measure of IE from satellite retrievals. The first method, (18), represents the aerosol effect on cloud microphysics and involves retrieving r_e from mid-IR channels. The second method, (23), represents the effect of aerosol on cloud albedo and involves retrieving ρ from visible channels. These two methods are independent from a remote sensing perspective but should give the same value for IE provided the present assumptions (e.g., constant LWP) hold (see section 3.2). Additionally, differentiation of (20) with respect to τ_d gives

$$\frac{d \ln \rho}{d \ln \tau_d} = (1-\rho), \tag{24}$$

and dividing (23) by (24) results in

$$\frac{d \ln \tau_d}{d \ln \tau_a} = \frac{1}{3}\left[\frac{a_1}{b_1} + \frac{a_2}{b_2} + \frac{a_3}{b_3}\right] = \mathrm{IE}. \tag{25}$$

Thus (18), (23), or (25) provide a measure of the indirect effect that is based on an empirical description of aerosol-cloud interactions (equation (11)) and which can easily be tested by quantities retrieved from satellite data. Furthermore, by using (18) we can use a simple parcel model to explore theoretically the physical parameters affecting the strength of the indirect effect. The modeling effort can test the effect of parameters not readily available from satellite observations, including the size distribution and hygroscopicity of the aerosol.

3. Data Analysis

3.1. Satellite and Water Vapor Data

The study uses AVHRR images at 1 km resolution to test the theoretical formulation of the previous section and to investigate the indirect effect in a biomass burning region. The study region over South America covers the area from −20°S to 5°N, −45°W to −70°W. Data from both the 1987 and the 1995 burning seasons (August through September) are analyzed in a consistent fashion following the methodology of *Kaufman and Nakajima* [1993] and KF97. AVHRR analysis yields products such as drop effective radius r_e, reflectance at 0.64 μm ρ, smoke optical depth τ_a, and cloud top temperature T_c. Products are spatially averaged to obtain mean quantities on a 1° × 1° grid. Cloud fraction is also calculated for each grid square.

In addition to AVHRR data the Goddard Data Assimilation Office (DAO) provides analyzed, daily, coarse vertical resolution temperature and specific humidity profiles as well as total column precipitable water vapor PWV. The horizontal spatial resolution in 1987 is 2.5° × 2.5°, increasing in 1995 to 1° × 1° over the entire region. Following KF97, a water vapor correction in the 3.75 μm channel was introduced above cloud to improve the accuracy of the retrieved cloud droplet radii. However, in this study the water vapor column above the cloud level is determined from the DAO data. Previously, it was based on monthly mean values of radiosonde stations in the region with the majority of the stations occurring in the south, leaving a paucity of data in the north. To evaluate the DAO water vapor data, the values of PWV were compared with data from Sun photometers at two Aerosol Robotic Network (AERONET) stations in the region of interest [*Holben et al.*, 1998]. The Sun photometers provide hourly and daily averaged values of PWV. In Figure 3, PWV data from the Sun photometers in Cuiaba (16°S, 56°W) and Brasilia (16°S, 48°W) are compared to DAO PWV data. A correlation coefficient of 0.84 gives reasonable confidence in the DAO PWV data. The finer horizontal and temporal resolution of the DAO data are a significant improvement over the monthly mean data used by KF97, both in terms of water vapor correction above the clouds and in characterizing the total PWV of the column.

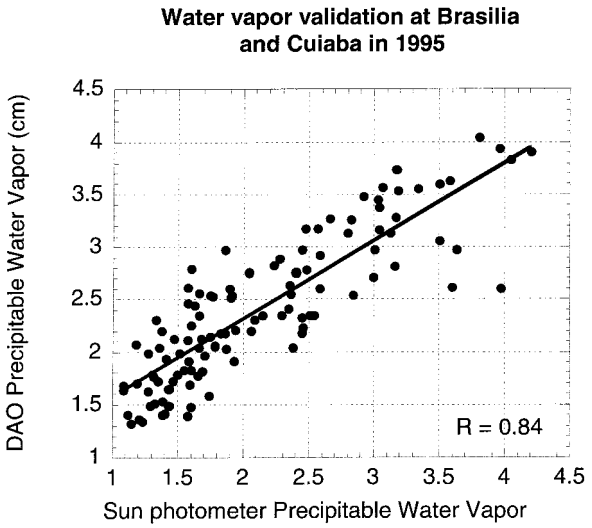

Figure 3. Comparison of PWV data derived from Sun photometers and DAO-derived PWV at Cuiaba and Brasilia. The correlation coefficient is 0.84.

Plate 1 shows the seasonal means of some of the variables derived from daily AVHRR images and DAO water vapor. The PWV is obtained from the DAO on a coarser resolution grid in 1987. From Plate 1 we see a north-south gradient in water vapor in both years but different spatial patterns in the distribution of smoke and clouds. In 1987 the smoke also followed a north-south gradient, but in 1995, the smoke gradient is more east-west, although the far north is comparatively clean in both years. The cloud fraction distribution also shows an interannual variability. These year-to-year changes are attributed to changes in cultural burning practices as well as variability in the average circulation patterns over the region.

3.2. Testing the Link Between Data Analysis and Modeling

The daily 1° × 1° data are aggregated and sorted according to smoke optical thickness. Cloud properties are included for all clouds within the broad temperature range of 270–290 K. Figure 4 shows r_e versus τ_a and ρ versus τ_a over the entire region for the 1995 data set. Increases in τ_a translate to significant decreases in r_e, and increases in ρ for $\tau_a < 0.4$, but

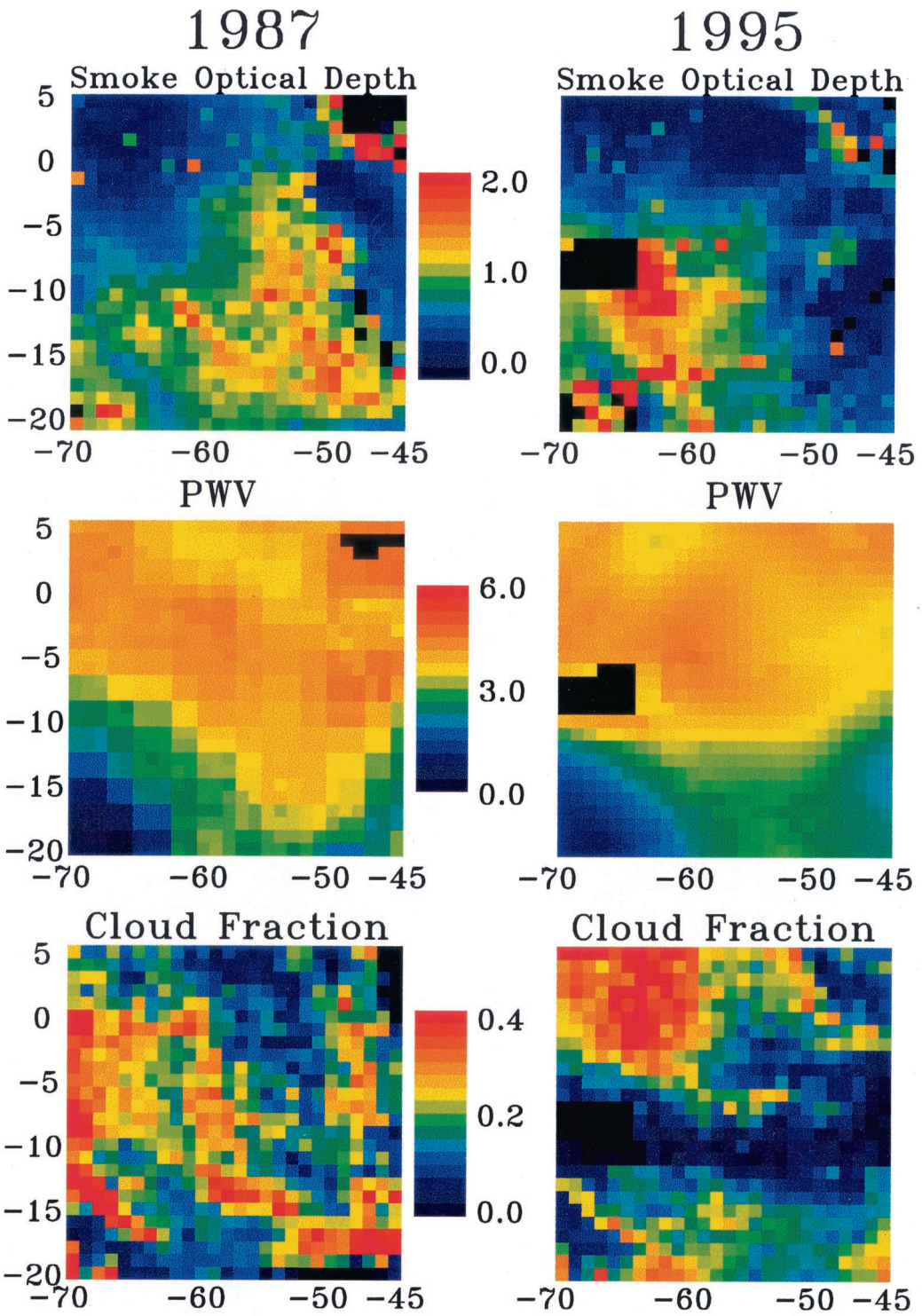

Plate 1. Seasonal mean values of τ_a, PWV, and cloud fraction based on daily AVHRR images and DAO water vapor.

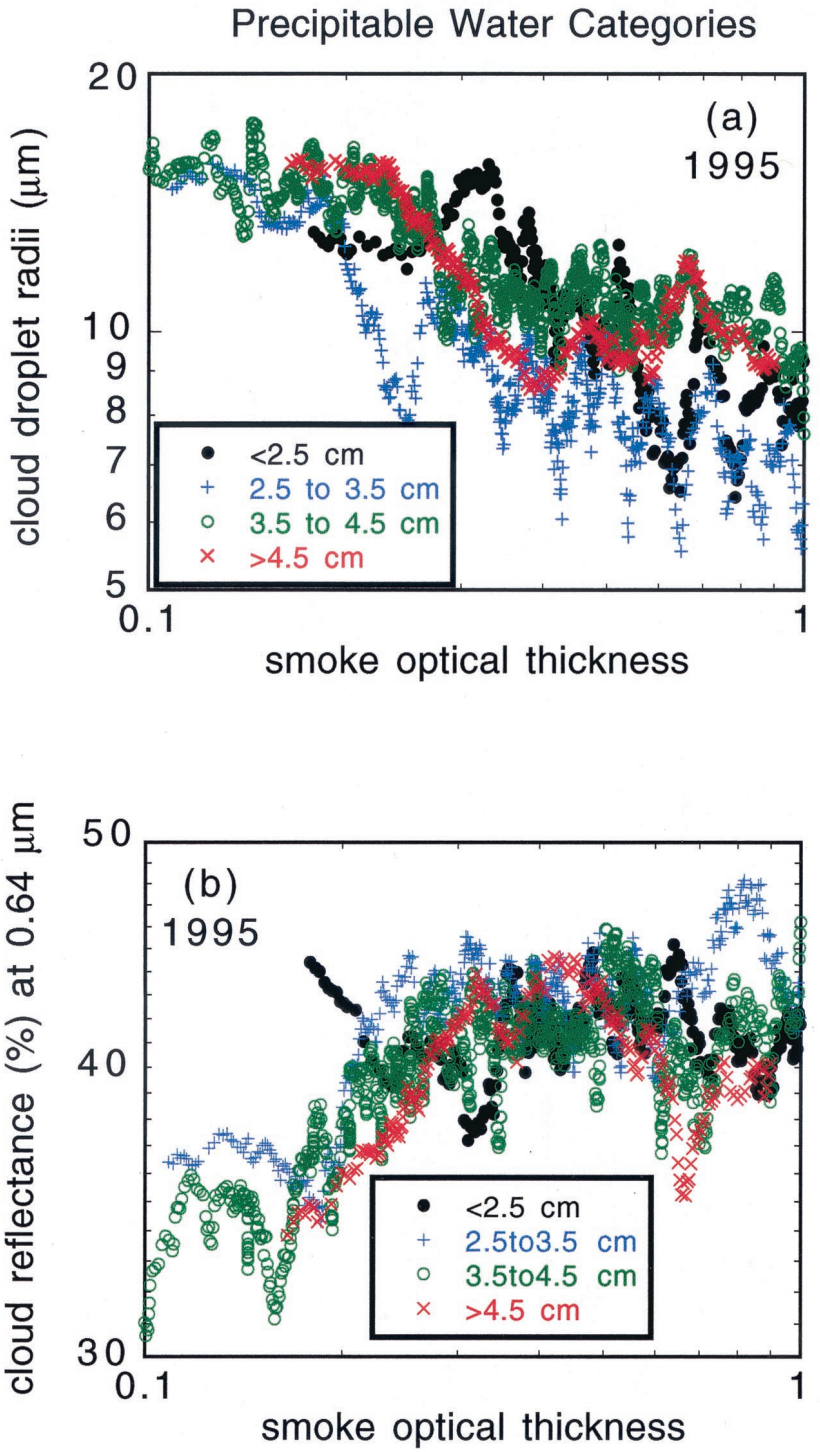

Plate 2. (a) Drop radius r_e and (b) cloud reflectance ρ at 0.64 μm as a function of τ_a for the different PWV zones and for 1995.

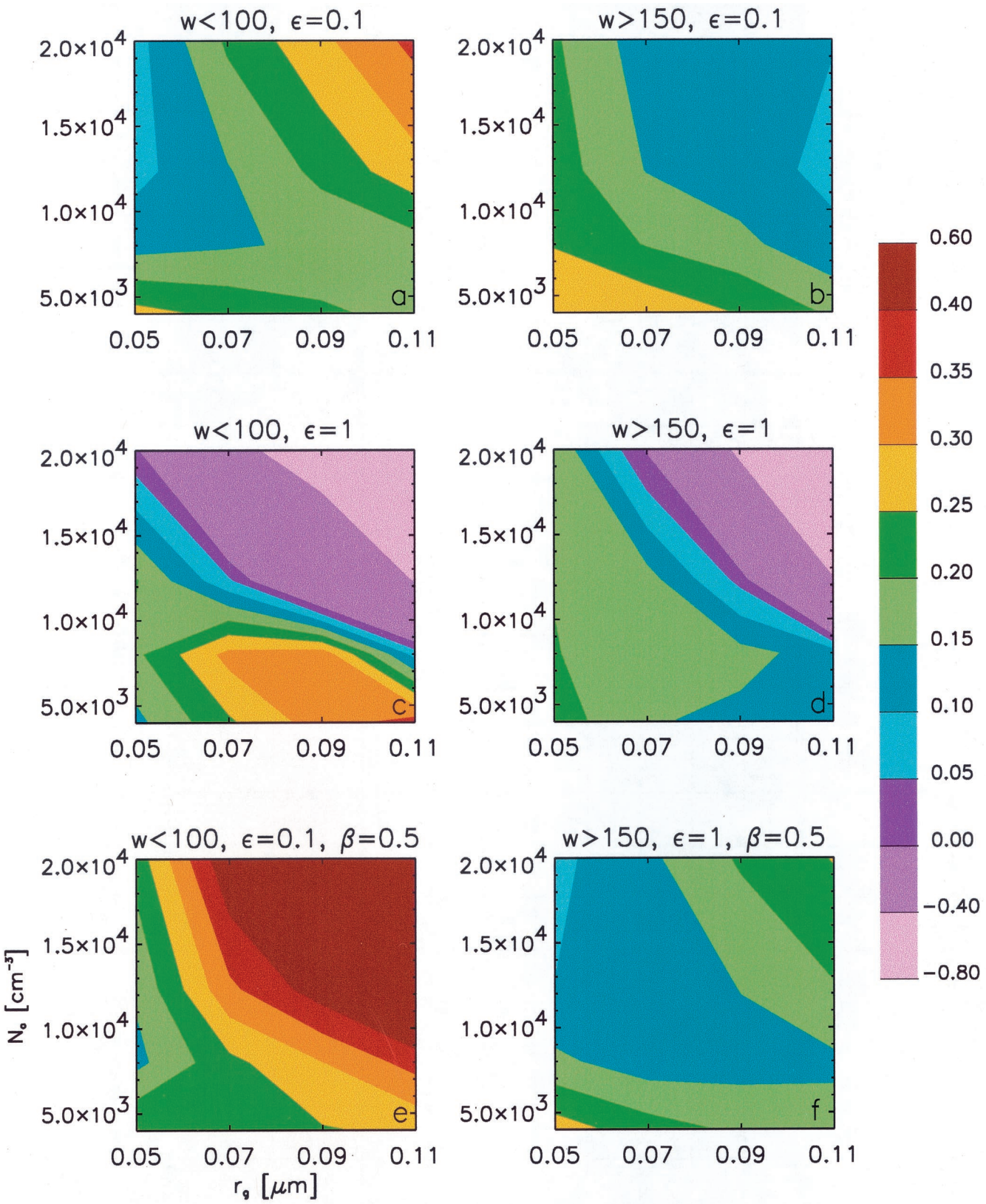

Plate 3. Contour plots of IE in N_a, r_g space where the regression (equation (11)) has been applied for limited ranges of N_a and r_g; w is vertical velocity; ε is a measure of the amount of soluble material in the particles; and β is a measure of how close to adiabatic the clouds are.

thereafter, the change is negligible. In the KF97 analysis of the 1987 data a similar relationship between the cloud variables, r_e and ρ, and smoke τ_a is found, but the saturation in signal tended to occur at a higher $\tau_a = 0.8$.

A least squares linear fit is applied to the sorted data of Figure 4 in the range of $0.10 < \tau_a < 1.00$. The slope of this linear fit is a measure of the strength of the indirect effect corresponding to (1) for the r_e versus τ_a relationship. Multiplying the slope by τ_a/r_e puts the measurement in the form of (2) and eliminates systematic biases introduced by either the aerosol or the cloud retrieval algorithms. Furthermore, the normalized slope derived from the AVHRR data analysis corresponds directly to the modeling variable IE of (2) or (18). A similar analysis applied to the ρ versus τ_a relationship corresponds directly to (23). Thus we have a link between the modeling formulation and the AVHRR data analysis.

We test this link by calculating IE from the data using the two independent methods presented by either (18) or (23),

$$\mathrm{IE}^* = \frac{1}{(1-\rho)} \frac{d \ln \rho}{d \ln \tau_a}. \tag{26}$$

In each year, 1987 and 1995, the data are divided into three latitudinal bins based on combinations of climatic variables. The north has high PWV and little smoke. The middle section is high in both smoke and PWV, while the south is dry and smoky. Each year, in each latitude bin, the data are sorted according to τ_a, a linear fit is applied to the proper range of data, and IE and IE* are calculated. The relationship between the two independent calculations of IE is shown in Figure 5. The mean values for each year and latitude zone are given in Table 3. There is a relationship between the independent calculations with a correlation coefficient of 0.56. The difference between these two estimates of IE could, at least partially, be associated with feedbacks of microphysics to LWP which are not considered in the current work. Excluding the outlying point at negative IE* improves the correlation to 0.78. Best fit lines to the data points are drawn for the purely scattering case (equation (23)) as well as for a case for which the cloud single-scattering albedo $\omega_o < 1$ [*Stephens*, 1994, page 311]:

$$\rho = \gamma_+ \gamma_- [e^{\kappa \tau_d} - e^{-\kappa \tau_d}]/\Delta(\tau_d), \tag{27}$$

where

$$\gamma_\pm = 1 \pm (1 - \omega_o) D/\kappa,$$

$$\Delta(\tau_d) = \gamma_+^2 e^{\kappa \tau_d} - \gamma_-^2 e^{-\kappa \tau_d},$$

$$\kappa = \{(1 - \omega_o) D[(1 - \omega_o) D + 2\omega_o b]\}^{1/2},$$

where D is the "diffuseness" of the radiation field (assumed = 2), and $b = (1 - g)/2$. Note that when $\omega_o = 0.98$, the best fit line to the data points lies somewhat closer to the theoretically predicted 1:1 line. Because numerous assumptions have been made in arriving at this figure, it is not suggested that ω_o can be derived from this analysis but rather that it is likely that there is an absorbing component in the aerosol. This simple test

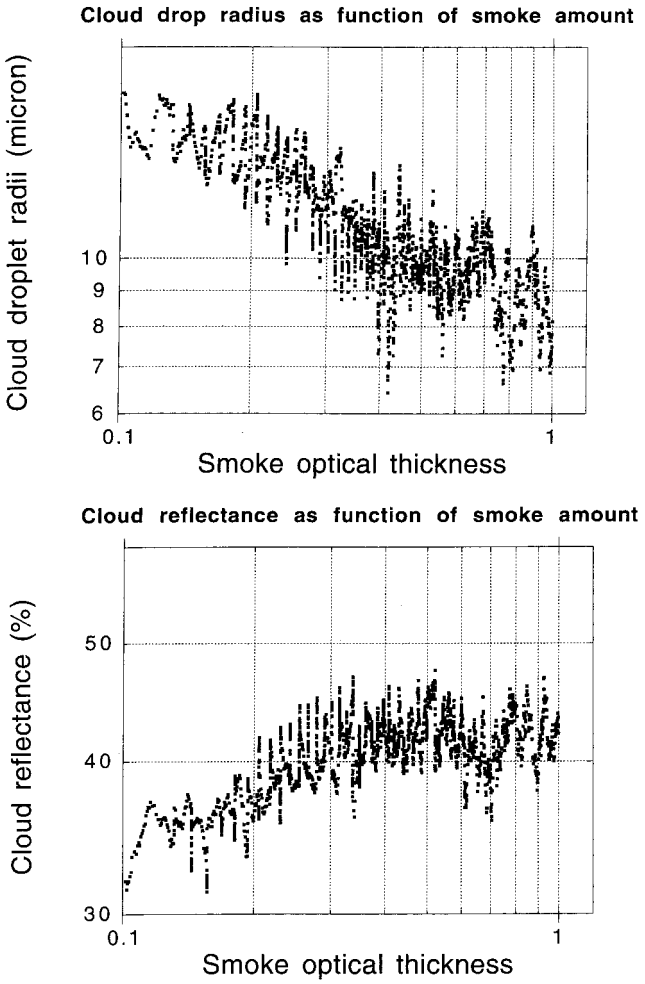

Figure 4. This shows r_e versus τ_a and ρ versus τ_a over the entire region for the 1995 data set. Note the saturation in r_e and ρ at large τ_a.

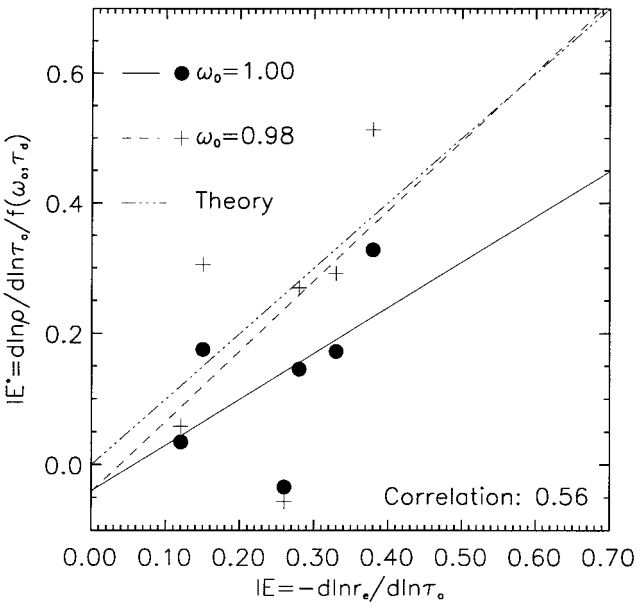

Figure 5. Indirect effect (IE) as calculated using equation (18) based on r_e retrieval in the mid-IR channels, and an independent calculation of IE (IE*) based on equation (23) which retrieves ρ from visible channels. The circles and solid line (best fit to the data) are for the purely scattering case (equation (23)), whereas the pluses and dashed line are for the solution when $\omega_o = 0.98$. Theory predicts a 1:1 relationship between the two parameters. Note that an absorbing component brings the slope of the best fit line closer to theory.

Table 3. Satellite Data Sorted According to Year and Latitudinal Zone and for Cloud Top Temperature in the 270–290 K Range[a]

Zone	Number of Samples	$\tau_{a,\min}$	$r_{e,\min}$, μm	$\bar{\tau}_a$	PWV, cm	CF	IE	IE*
			1987					
0°–5°N	347	0.15	13	0.40	4.0	0.25	0.33	0.17
1°–10°S	509	0.22	13	0.82	4.0	0.15	0.28	0.15
11°–20°S	165	0.27	9	1.16	2.5	0.17	0.15	0.18
			1995					
0°–5°N	699	0.10	18	0.31	4.0	0.21	0.38	0.33
1°–10°S	818	0.11	7	0.50	3.9	0.13	0.12	0.03
11°–20°S	626	0.14	9	0.78	2.6	0.11	0.26	−0.03

[a]Mean quantities represent average conditions in the latitude zone. IE and IE* are calculated for the subset of samples (as indicated by number of samples) for which $\tau_a < 1.0$. The following definitions apply: $\tau_{a,\min}$ is the minimum aerosol optical depth; $r_{e,\min}$ is the drop effective radius at $\tau_{a,\min}$; $\bar{\tau}_a$ is the average τ_a in the zone; PWV is the precipitable water vapor in centimeters; CF is the cloud fraction of all squares in the zone; IE is defined by equation (3); and $IE^* = 1/(1 - \rho)d \ln \rho/d \ln \tau_a$.

provides confidence that we have established a working framework for linking the modeling with the data analysis.

3.3. Testing the Dependence of the Indirect Effect on Water Vapor

The DAO data are used together with the AVHRR data to examine the hypothesis that precipitable water vapor plays a role in influencing the pattern of the indirect effect (KF97). The data were resorted according to PWV values and then divided into four categories, regardless of latitude. Table 4 gives the mean values in each PWV category, and Plate 2 shows drop radius and cloud reflectance at 0.64 μm as a function of τ_a for the different categories for 1995. Contrary to the analysis of KF97, there is no systematic difference in results as a function of PWV. This is confirmed by the poor correlation between IE and PWV in Tables 3 and 4.

KF97 never directly correlated the indirect effect with precipitable water vapor. They correctly identified the latitudinal dependence of the indirect effect, which appears clearly in Table 3 in both years of data, and used latitude as a proxy for water vapor. However, the limited water vapor data available to KF97 are misleading in their spatial distribution. A reanalysis of the 1987 data set, using the DAO values of PWV, shows that although the north is wet and the south is dry, the spatial gradient in between does not correlate with the strength of the indirect effect. There is a latitudinal dependence of IE in South America, but it is not necessarily directed by PWV.

3.4. Testing the Dependence of the Indirect Effect on Smoke Amount

The most noteworthy feature of Table 3 is the large positive value of IE = 0.38 in the 0°–5°N zone (1995) and the steady increase in mean τ_a from North to South. There is a trend for IE to decrease with increasing τ_a except for one data point (1°–10°S, 1995), which has a much smaller IE than other points with similar τ_a. The question remains whether smoke characteristics alone, as represented by τ_a, are sufficient to modulate the strength of the indirect effect. For this answer we return to the modeling analysis.

4. Interpretation of the Observations Using the Model

By looking to the model to interpret the data it should be stressed that the nature of the model, and its incomplete representation of natural processes, as well as the approximate form of the regressions is such that we do not intend for this analysis to be taken as quantitatively correct but rather as an indicator of the relative change in the IE for different conditions. Where there is a robust model result, we use the model to interpret the observations but recognize that other explanations could be possible. Despite these caveats, we feel it is important to make this step if we are to improve our understanding of smoke-cloud interactions.

Table 2 gives the values of a_n and IE based on (18) for

Table 4. Satellite Data Sorted According to Year and Precipitable Water Vapor (PWV) Bins With Analysis Consistent with Table 3

PWV, cm	Number of Samples	$\tau_{a,\min}$	$r_{e,\min}$, μm	$\bar{\tau}_a$	IE	Latitude
			1987			
<2.5	110	0.27	8	1.01	0.06	15°S
2.5–3.5	183	0.17	13	0.87	0.39	7°N
3.5–4.5	573	0.15	13	0.74	0.34	4°S
>4.5	155	0.18	13	0.70	0.34	3°N
			1995			
<2.5	298	0.18	13	0.75	0.43	16°S
2.5–3.5	521	0.11	15	0.64	0.39	10°S
3.5–4.5	1101	0.10	16	0.45	0.26	2°S
>4.5	223	0.17	16	0.43	0.32	1°S

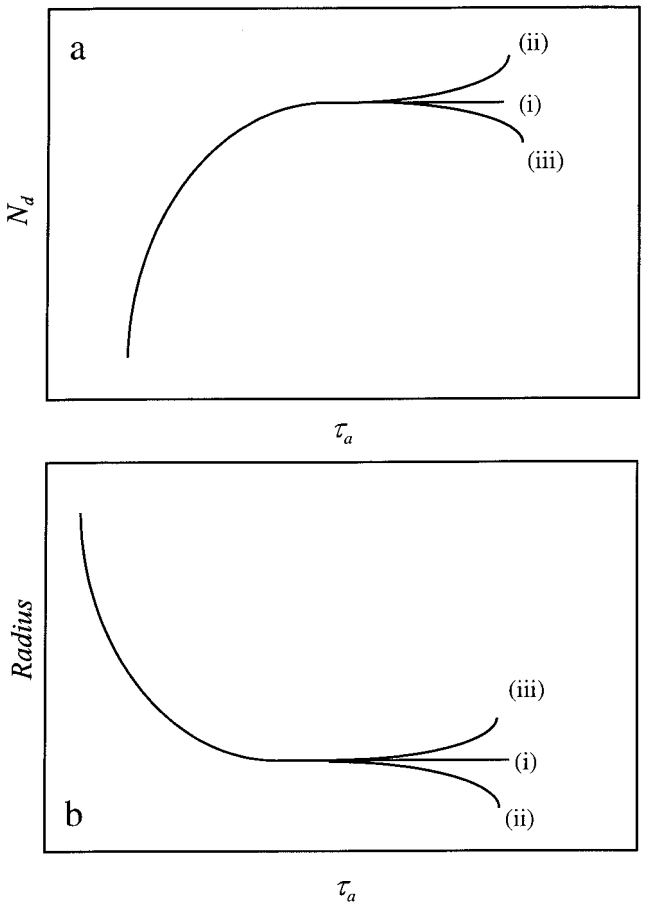

Figure 6. Qualitative illustration of the three identified responses of (a) drop number N_d to increasing aerosol loading and (b) r_e to increasing aerosol loading. Response *i*, saturation in N_d (r_e); *ii*, saturation in N_d (r_e), followed by an increase (decrease) in N_d (r_e); *iii*, saturation in N_d (r_e) followed by a decrease (increase) in N_d (r_e). All scales are linear.

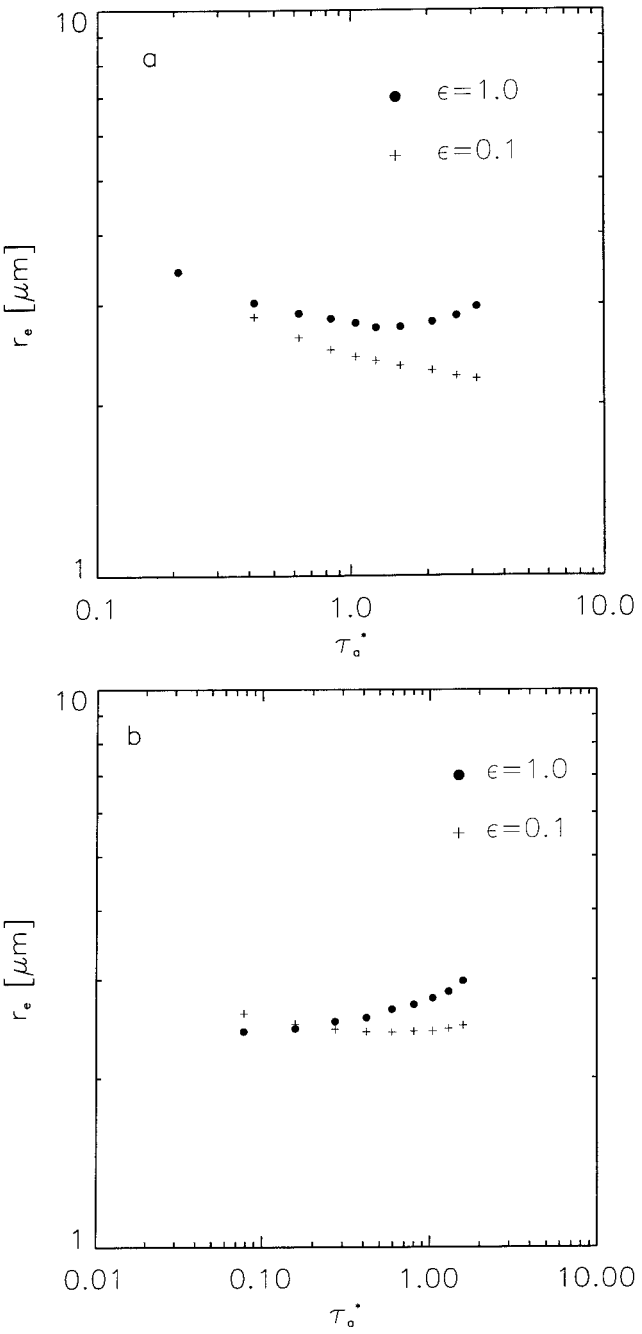

Figure 7. Model calculations of r_e for given τ_a^*, where τ_a^* is arbitrarily defined as τ_a for a homogeneous smoke layer of 500 m depth. Calculations are for $\sigma = 2$, and $w = 300$ cm s^{-1}. (a) for $r_g = 0.1$ μm and variable N_a; (b) for $N_a = 10{,}000$ cm^{-3} and variable r_g. At large N_a, or r_g, the IE (slope of the curve) is negligible and may even be negative, especially for $\varepsilon = 1$.

different broad ranges of aerosol input parameters, as well as different dynamical forcings. We note that unlike (7), where $0 \leq \text{IE} \leq 0.33$, (18) yields no clear indication of the upper and lower bounds of IE because the signs of a_2 and a_3 are not known. Thus IE can be greater than 0.33, and under some circumstances, IE is negative (see section 4.1).

The regressions in Table 2 over a broader parameter space reveal interesting dependences of IE on a_n. For example, weak IE is primarily reflected in small or even negative values of a_2 (suggesting that an increase in r_g has little effect on or even reduces N_d), and strong negative values of a_3 that imply that a broad smoke aerosol spectrum has sufficient large particles to suppress supersaturation, and therefore N_d. The latter result is analogous to that derived from *Twomey*'s [1959] analytical equation (12) which shows that decreases in the k parameter (akin to increasing σ) decrease the dependence of N_d on N_a (C in his case) and increase the dependence of N_d on w.

To supplement Table 2, Plate 3 shows contour plots of IE in (N_a, r_g) space where the regression (equation (11)) has been applied to limited ranges of N_a and r_g. By parsing the model output, one can detect trends in the coefficients and derived IE, which can be useful for interpreting observations for similar conditions. The fact that a_n change when the model output is parsed into smaller ranges of size distribution parameters is not unexpected. Again, we point to *Twomey*'s [1959] solution (equation (12)) which shows that the dependence of N_d on aerosol concentration and w is dependent on the aerosol size distribution parameter k.

4.1. Identification of Three Primary Responses

On the basis of Plate 3 and Table 2, three primary responses of cloud microphysics to aerosol parameters and updraft are

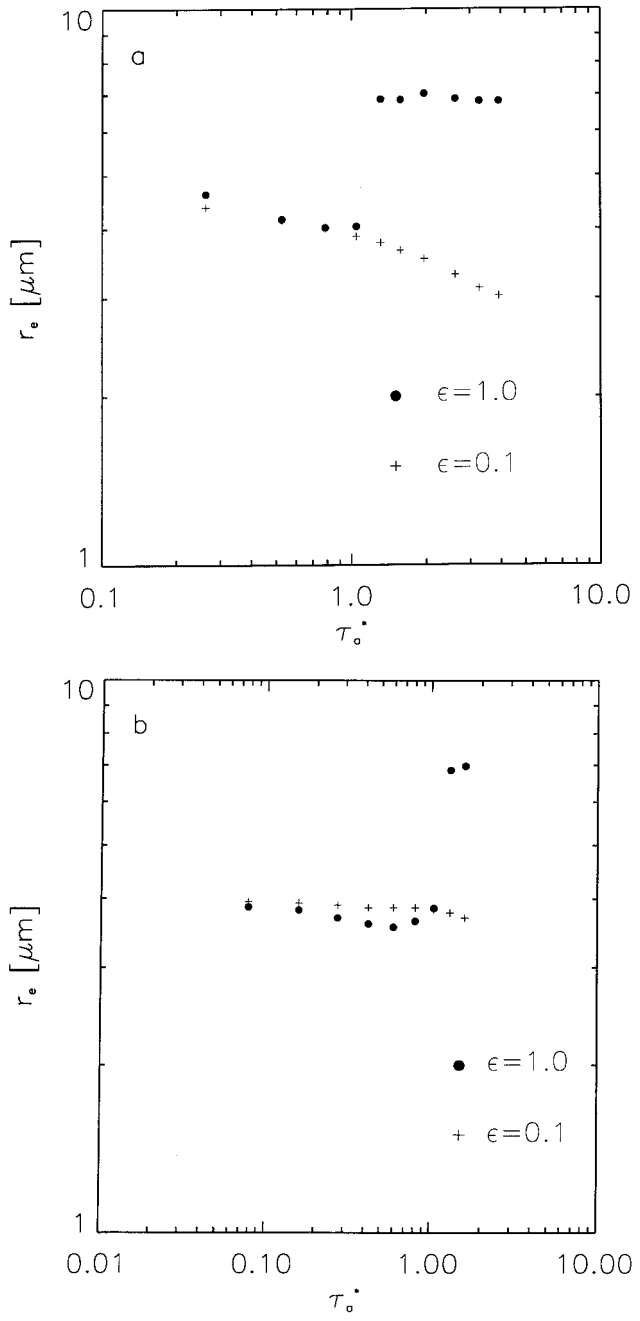

Figure 8. As in Figure 7 but for calculations at $\sigma = 2$ and $w = 50$ cm s^{-1}: (a) for $r_g = 0.11$ μm and variable N_a; (b) for $N_a = 10{,}000$ cm^{-3} and variable r_g. For $\varepsilon = 1$, r_e increases at large N_a, or r_g implying a negative IE. This is related to competition for vapor resulting in the evaporation of droplets. For $\varepsilon = 0.1$, r_e is fairly constant with increasing N_a or r_g but tends to decrease more sharply at very large N_a or r_g.

identified. A conceptual plot of these three responses is given in Figure 6.

4.1.1. (*i*) Cloud droplet concentrations increase with increasing aerosol loading, followed by saturation in the response at high concentrations. When w is large, there is a tendency for IE to decrease with increasing N_a and r_g (Plate 3b). At large w, supersaturation production is adequate, and for low N_a and r_g, there is a strong correlation between N_d and smoke loading (large IE). However, as N_a and r_g increase, competition for vapor hinders growth, fewer and fewer new particles can be activated, and IE becomes progressively smaller. (When N_a is very large, the competition for vapor among particles is enormous and the definition of what constitutes a drop, rather than a haze particle, is somewhat arbitrary. In our analysis we do not adhere to the strict definition of activation but assume that particles with radii greater than 1 μm are activated drops, to facilitate comparison with in situ measurements of cloud droplets using forward light scattering probes (FSSP) (particle measuring systems). In some cases this may underestimate the number concentration of optically active haze particles/drops [see also *Reid et al.*, 1999].) This implies that N_d and r_e become progressively less dependent on τ_a; that is, they reach saturation. This result is consistent with observations from much cleaner conditions [e.g., *Martin et al.*, 1994], which indicate a saturation in N_d when N_a increases above some threshold.

4.1.2. (*ii*) Cloud droplet concentrations increase with increasing aerosol loading, saturation in the response (as in *i*), followed by an increase in droplet concentrations. When w is small, there are two regions of higher IE: one at small N_a and r_g, and a second at large N_a and r_g, with a minimum in between (Plate 3a). As in *i*, there is a strong correlation between N_d and aerosol loading at low N_a and r_g which results in higher IE. However, because at small w the system is limited by low supersaturation production, increases in N_a and r_g result in strong competition for available vapor and a more rapid decrease in IE. A close analysis of the model output shows that further increases in N_a and r_g create a situation where large particles suppress supersaturation at the early stages of activation [*Ghan et al.*, 1998; *Feingold and Kreidenweis*, 2000] and prevent many of the smaller particles from activating; these smaller particles are especially difficult to activate when $\varepsilon = 0.1$. The absence of smaller drops, which are efficient at taking up water vapor, allows a slower but sustained activation of larger particles and results in larger IE. Note that if w were large enough, the largest particles would not be able to suppress activation of many of the smaller particles, which is why the secondary peak is not observed at the higher w. We are unaware of observational evidence for these two regions, but note that this implies that there may be potential for further activation after the system is saturated, i.e., beyond the point of IE = 0.

4.1.3. (*iii*) Cloud droplet concentrations increase with aerosol loading, saturation in response (as in *i*), followed by a negative response as intense competition for vapor evaporates the smallest droplets. When particles are very hydrophilic ($\varepsilon = 1$), activation is facilitated, and competition for vapor is so strong that after the response of the cloud to the addition of particles has saturated (IE $\approx$ 0), the addition of more particles results in a steady evaporation of smaller drops and negative IE. This indicates an unexpected increase in r_e (or decrease in N_d) with increasing τ_a. The largest negative values of IE occur at large N_a and large r_g (Plates 3c and 3d). Again, we know of no observational evidence for negative IE, but note that if it does occur in nature, it constitutes an interesting microphysical feedback; at very high aerosol loadings, competition for available water vapor may act to reverse the general tendency for drop number to increase with increasing aerosol concentration.

To examine this more closely, Figure 7 illustrates individual model calculations of r_e for given τ_a^*, where τ_a^* is arbitrarily defined as τ_a for a homogeneous smoke layer of 500 m depth.

Calculations are performed at fixed $\sigma = 2$, and $w = 300$ cm s^{-1}; individual points pertain to the values of N_a (Figure 7a) and to the values of r_g (Figure 7b) in Table 1. In the case of $\varepsilon = 0.1$, the slope of $\log r_e$ versus $\log \tau_a$ decreases gradually with increasing τ_a (or N_a). For $\varepsilon = 1.0$, the slope tends to zero and then reverses to a positive slope, or negative IE. Figure 8 further exemplifies the negative IE response by examining an equivalent simulation at low w. The results for $\varepsilon = 0.1$ in Figure 8 also capture the increase in IE at high τ_a^*, which is indicated by response (*ii*).

The cases including entrainment (Plates 3e and 3f) illustrate a dependence of IE on N_a and r_g similar to *ii* with two maxima in IE. Entrainment of dry air enhances the effects outlined in *ii* by forcing the numerous small droplets to evaporate; larger drops are more robust to evaporation and may even grow at the expense of small drops. The highest modeled IE occur under these conditions when w is small. Table 2 supports this argument by showing that entrainment results in larger, and positive values of a_2 and a_3; that is, the model indicates that increases in r_g and σ will increase IE by supplying larger droplets that are more robust to the entrainment drying.

Plate 4 plots satellite-derived values of IE and places them in N_a, r_g parameter space as in Plate 3. Two different values of r_g have been assumed, and N_a has been derived from τ_a assuming a fixed $\sigma = 1.82$. The derived values of N_a for assumed r_g depend primarily on σ and on the assumed depth of the smoke layer. If σ and/or the depth of the smoke layer were assumed smaller, the derived N_a would be larger, and vice versa; for this reason we do not attempt to match the same N_a, r_g values as in Plate 3 but concentrate rather on observed trends. In general, model-derived values of IE are consistent with the observed values. In the north the satellite-derived IE of 0.38 in 1995 is large and only exceeded by modeled values of IE in Plate 3e for conditions of low w, low solubility, and subadiabatic conditions. In 1987 there is a monotonic decrease in IE with increasing N_a (and τ_a) which is akin to the model results in Plate 3b. However, in 1995 the data points have larger IE at both lower and higher N_a (or τ_a), with a smaller value at the intermediate value of N_a (or τ_a). This follows the pattern for response *ii* (Plates 3a and 3e). We note that the 1995 burning season was characterized by an anomalously strong inversion [*Nobre et al*., 1998], and if we assume that this resulted in weaker convection, comparison of the 1995 data with the weaker updrafts of Plates 3a and 3e is appropriate. The consistency between Plate 4b and response *ii* does support the idea that response *ii* actually occurs in real clouds, but clearly, more data would be required to place this hypothesis on firmer ground.

4.2. Dependence of the Indirect Effect on τ_a

The modeling results indicate that τ_a is not necessarily a sufficient determinant of IE. This conclusion is arrived at by calculating IE for subsets of lognormal parameter space (Table 1), determining the τ_a range given by these parameters, and then calculating IE on a new subset of the model output that encompasses the very same τ_a range, but with no restrictions on the lognormal parameters. (See table entries labeled "equivalent τ_a" in Table 2.) The exercise determines to what extent τ_a is a good proxy for the detailed size distribution information. For example, Table 2 indicates that a very weak indirect effect (IE = 0.08) is obtained when $r_g > 0.08$ μm, $N_a > 5000$ cm^{-3}, and $w \geq 200$ cm s^{-1}. If the model output is then resorted according to the τ_a range prescribed by those same parameters ($r_g > 0.08$ μm and $N_a > 5000$ cm^{-3}), but this time with no restriction on the lognormal parameter space, a much more significant indirect response of IE = 0.19 is obtained. Similarly, when the IE has a significant value of 0.30 for $r_g \leq 0.08$ μm, $N_a \leq 5000$ cm^{-3}, and $w \leq 200$ cm s^{-1}, the "equivalent τ_a" yields a much reduced indirect effect (IE = 0.22). To first order τ_a is probably a good measure of IE, but this analysis suggests that the details of the aerosol size distribution, even when parameterized with a simple lognormal function, may be important.

One should bear in mind that the parameter space for aerosol reflects the large number concentrations of particles found in smoke (up to 2 orders of magnitude greater than typical continental concentrations not prone to smoke) and that the present analysis may not be applicable to those typical scenarios. Similar analyses could easily be performed for much cleaner conditions than those examined here.

4.3. Susceptibility

The tendency for the indirect effect to be strongest at the lowest smoke optical depths is analogous to the concept of susceptibility S introduced by *Platnick and Twomey* [1994]:

$$S = \left.\frac{d\rho}{dN_d}\right|_{\text{const LWC}} = \frac{\rho(1-\rho)}{3N_d}, \tag{28}$$

or simply,

$$\frac{d \ln \rho}{d \ln N_d} = \frac{(1-\rho)}{3}. \tag{29}$$

Equation (28) predicts that clouds forming in cleaner environments (larger drops, and lower ρ) will have a stronger response to the addition of drops than equivalent, more reflective clouds. For a very reflective cloud with $\rho = 1$, the response is zero. There is a fundamental difference between S, as defined by (28), and IE, as defined by (2); S relies on a measure of N_d, while IE casts the change in cloud properties (in this case, r_e, or ρ, in the case of (23)) in terms of a bulk aerosol property (τ_a). Susceptibility thus short-circuits the complex interaction between cloud droplet formation and aerosol properties, while IE must include them directly. Once equations for N_d in terms of aerosol parameters have been established (equations (10) and (11)), calculation of S is straightforward.

5. Summary

Analysis of aerosol-cloud interaction, or the "aerosol indirect effect," has been undertaken using extensive satellite remote sensing measurements in the biomass burning regions of Brazil. Retrievals of cloud drop radius, cloud reflectance, and smoke optical depth enable assessment of the effect of smoke aerosol on cloud microphysical and optical properties [*Kaufman and Nakajima*, 1993]. This is usually described as the change in drop radius as a function of the change in smoke optical depth. KF97 suggested that PWV might be an additional parameter determining the indirect effect. The current analysis of 2 years of data does not support this hypothesis. Analysis indicates that the cloud drop response to aerosol is greatest in the north of Brazil, where aerosol optical depth is smallest, and tends to decrease as one moves southward, and as aerosol optical depth increases. Saturation in this response occurs at an aerosol optical depth of 0.8 in 1987 and 0.4 in 1995.

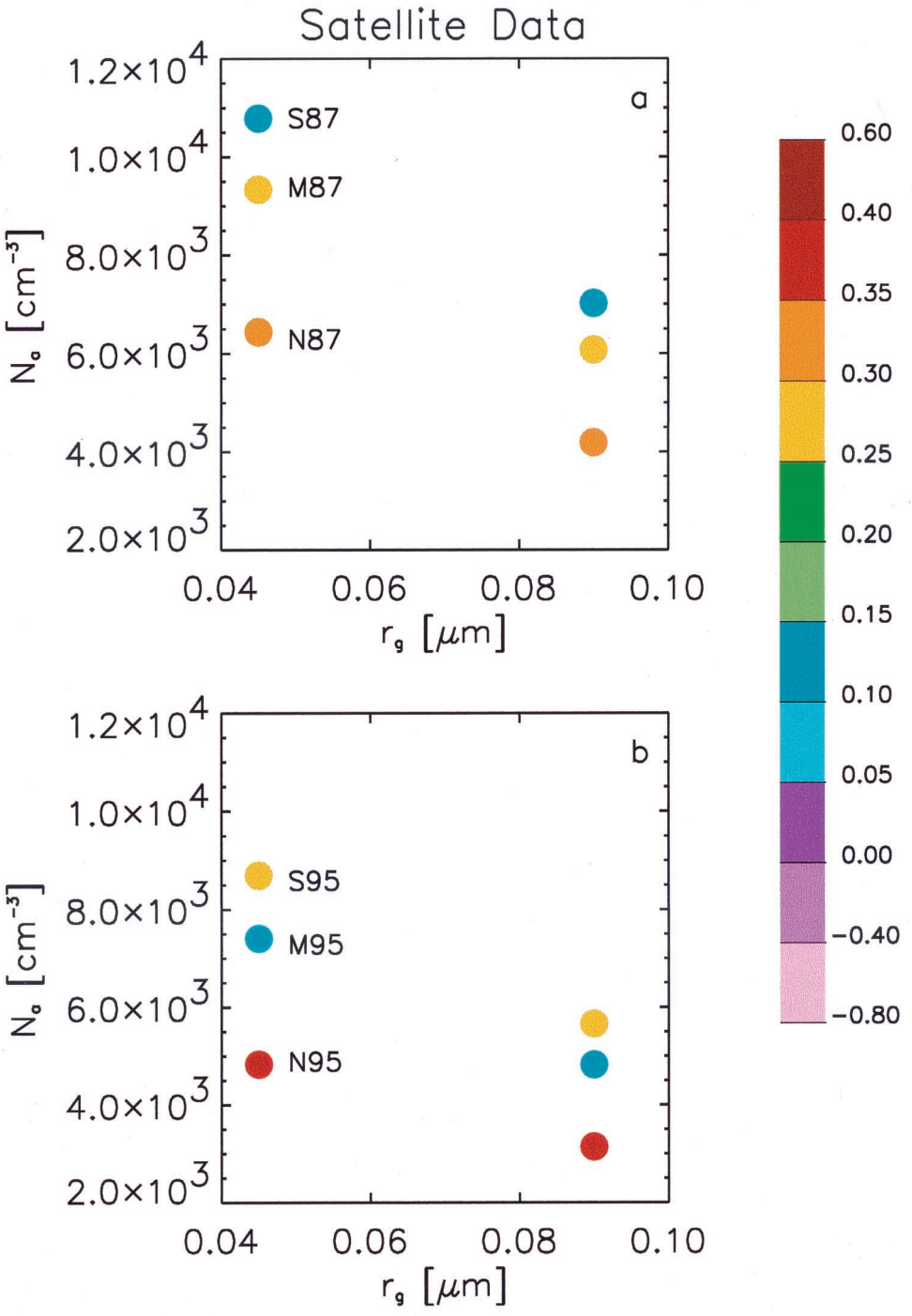

Plate 4. Satellite-derived IE in N_a, r_g space assuming two different values of r_g, and with N_a derived from the measurement of τ_a, and an assumed aerosol distribution breadth. The circles are labeled according to year (1987 or 1995) as well as according to latitudinal band: N (North), M (Middle), and S (South). (a) for 1987 data, (b) for 1995 data.

An analytical/modeling approach has been taken to unify the descriptions of aerosol-cloud interaction and to assist in evaluation of the indirect effect. This new framework extends *Twomey*'s [1974] representation to include the effects of aerosol size distribution parameters. It retains the basic assumptions of a homogeneous cloud and compares aerosol effects for clouds of similar liquid water content. As such, it should be seen as a tool to explore first-order effects of aerosol-cloud interaction. It does not include aerosol-radiative-dynamical feedbacks. It does show that variability in the observed saturation in indirect effect may be related to both dynamics, as well as aerosol size distribution and composition.

It is suggested that for remote sensing applications the indirect effect is best defined as a relative change in cloud drop size for a relative change in smoke optical depth since this alleviates measurement biases. A numerical model is used to generate the coefficients that quantify aerosol-cloud interaction. The model's incomplete description of this interaction

means that the most appropriate use of the model is to explore the relative importance of various aerosol parameters in determining cloud properties.

The new theoretical analysis is applied to the data analysis, and its utility in helping describe cloud response to smoke aerosol is demonstrated. Three primary responses are identified (Figure 6); the conditions under which each of these responses are to be expected are described in the text: (*i*) cloud droplet concentrations increase with increasing aerosol loading, followed by saturation in the response at very high concentrations; (*ii*) cloud droplet concentrations increase with increasing aerosol loading, saturation in the response (as in *i*), followed by an increase in response when sufficient large particles exist to quench supersaturation during the early stages of activation and prevent activation of smaller particles [*Ghan et al*., 1998; *Feingold and Kreidenweis*, 2000]; (*iii*) cloud droplet concentrations increase with aerosol loading, saturation in response (as in *i*), followed by a negative response as intense competition for vapor evaporates the smallest droplets. Thus we hypothesize that at very high mass loadings, the microphysical response to smoke may not be monotonic.

Despite the apparent relationship between optical depth and strength of the indirect effect in the satellite analysis, the modeling study points to a different conclusion. Because the activation process is so strongly dependent on the aerosol size distribution, hygroscopicity, and supersaturation production, the modeling study suggests that optical depth is not always an adequate surrogate for describing the strength of the indirect effect.

This analysis has also yielded a simple empirical equation describing the number of drops activated as a function of aerosol size distribution parameters (parameterized as a log-normal function) as well as vertical velocity (equation (11)). The coefficients that quantify droplet activation have been calculated using regression fits to the model output for a large range of parameter space. This equation could easily be applied as a drop activation algorithm in general circulation models [e.g., *Ghan et al*., 1993, 1997], but we caution that better accuracy can be attained when the coefficients are calculated over smaller sections of parameter space.

Acknowledgment. This research was supported under NASA grant 622-44-64-20.

References

Albrecht, B. A., Aerosols, cloud microphysics, and fractional cloudiness, *Science*, *245*, 1227–1230, 1989.

Arends, B. G., et al., Microphysics of clouds at Kleiner Feldberg, *J. Atmos. Chem*., *19*, 59–85, 1994.

Artaxo, P., E. T. Fernandes, J. V. Martins, M. A. Yamasoe, P. V. Hobbs, W. Maenhaut, K. M. Longo, and A. Castanho, Large-scale aerosol source apportionment in Amazonia, *J. Geophys. Res*., *103*, 31,837–31,847, 1998.

Bohren, C. F., Multiple scattering of light and some of its observable consequences, *Am. J. Phys*., *55*, 524–533, 1980.

Charlson, R. J., J. E. Lovelock, M. O. Andreae, and S. G. Warren, Oceanic phytoplankton, atmospheric sulphur, cloud albedo and climate, *Nature*, *326*, 655–661, 1987.

Charlson, R. J., S. E. Schwartz, J. M. Hales, R. D. Cess, J. A. Coakley Jr., J. E. Hansen, and D. J. Hofmann, Climate forcing by anthropogenic aerosols, *Science*, *255*, 423–430, 1992.

Coakley, J. A., Jr., R. L. Bernstein, and P. A. Durkee, Effect of ship-stack effluents on cloud reflectivity, *Science*, *237*, 1020–1022, 1987.

Conover, J. H., Anomalous cloud lines, *J. Atmos. Sci*., *23*, 778–785, 1966.

Feingold, G., and A. J. Heymsfield, Parameterizations of condensational growth of droplets for use in general circulation models, *J. Atmos. Sci*., *49*, 2325–2342, 1992.

Feingold, G., and S. M. Kreidenweis, 2000: Does cloud processing of aerosol enhance droplet concentrations?, *J. Geophys. Res*., *105*, 24,351–24,361, 2000.

Ghan, S. J., C. C. Chuang, and J. E. Penner, A parameterization of cloud droplet nucleation, part I, Single aerosol type, *Atmos. Res*., *30*, 197–221, 1993.

Ghan, S. J., L. R. Leung, R. C. Easter, and H. Abdul-Razzak, Prediction of cloud droplet number in a general circulation model, *J. Geophys. Res*., *102*, 21,777–21,794, 1997.

Ghan, S. J., G. Guzman, and H. Abdul-Razzak, Competition between sea salt and sulfate particles as cloud condensation nuclei, *J. Atmos. Sci*., *55*, 3340–3347, 1998.

Holben, B. N., et al., AERONET—A federated instrument network and data archive for aerosol characterization, *Remote Sens. Environ*., *66*, 1–16, 1998.

Kaufman, Y. J., and M.-D. Chou, Model simulations of the competing climatic effects of SO_2 and CO_2, *J. Clim*., *6*, 1241–1252, 1993.

Kaufman, Y. J., and R. S. Fraser, The effect of smoke particles on clouds and climate forcing, *Science*, *277*, 1636–1639, 1997.

Kaufman, Y. J., and T. Nakajima, Effect of Amazon smoke on cloud microphysics and albedo—Analysis from satellite imagery, *J. Appl. Meteorol*., *32*, 729–744, 1993.

Kaufman, Y. J., R. S. Fraser, and R. L. Mahoney, Fossil fuel and biomass burning effect on climate—Heating or cooling?, *J. Clim*., *4*, 578–588, 1991.

Kotchenruther, R., and P. V. Hobbs, Humidification factors of aerosols from biomass burning in Brazil, *J. Geophys. Res*., *103*, 32,081–32,089, 1998.

Leaitch, W. R., G. A. Isaac, J. W. Strapp, C. M. Banic, and H. A. Wiebe, The relationship between cloud droplet number concentrations and anthropogenic pollution: Observations and climatic implications, *J. Geophys. Res*., *97*, 2463–2474, 1992.

Leaitch, W. R., C. M. Banic, G. A. Isaac, M. D. Couture, P. S. K. Liu, I. Gultepe, and S.-M. Li, Physical and chemical observations in marine stratus during the 1993 North Atlantic Regional Experiment: Factors controlling cloud droplet number concentrations, *J. Geophys. Res*., *101*, 29,123–29,135, 1996.

Lohmann, U., and J. Feichter, Impact of sulfate aerosols on albedo and lifetime of clouds: A sensitivity study with the ECHAM4 GCM, *J. Geophys. Res*., *102*, 13,685–13,700, 1997.

Martin, G. M., D. W. Johnson, and A. Spice, The measurement and parametrisation of effective radius in warm stratocumulus clouds, *J. Atmos. Sci*., *51*, 1823–1842, 1994.

Nobre, C. A., L. F. Mattos, C. P. Dereczynski, T. A. Tarasova, and I. V. Trosnikov, Overview of atmospheric conditions during the Smoke, Clouds, and Radiation–Brazil (SCAR–B) field experiment, *J. Geophys. Res*., *103*, 31,809–31,820, 1998.

Novakov, T., C. Rivera-Carpio, J. E. Penner, and C. F. Rogers, The effect of anthropogenic sulfate aerosols on marine cloud droplet concentrations, *Tellus*, *Ser. B*, *46*, 132–141, 1994.

Platnick, S., and S. Twomey, Determining the susceptibility of cloud albedo to changes in droplet concentration with the advanced very high resolution radiometer, *J. Appl. Meteorol*., *33*, 334–347, 1994.

Pruppacher, H. R., and J. D. Klett, *Microphysics of Clouds and Precipitation*, Kluwer Acad., 954 pp., 1997.

Raga, G. B., and P. R. Jonas, On the link between cloud-top radiative properties and sub-cloud aerosol concentrations, *Q. J. R. Meteorol. Soc*., *119*, 1419–1425, 1993.

Reid, J. S., P. V. Hobbs, R. J. Ferek, D. R. Blake, J. V. Martins, M. R. Dunlap, and C. Liousse, Physical, chemical and optical properties of regional hazes dominated by smoke in Brazil, *J. Geophys. Res*., *103*, 32,059–32,080, 1998.

Reid, J. S., P. V. Hobbs, A. L. Rangno, and D. A. Hegg, Relationships between cloud droplet effective radius, liquid water content, and droplet concentration for warm clouds in Brazil embedded in biomass smoke, *J. Geophys. Res*., *104*, 6145–6153, 1999.

Remer, L., Y. J. Kaufman, B. N. Holben, A. M. Thompson, and D. McNamara, Biomass burning aerosol size distribution and modeled optical properties, *J. Geophys. Res*., *103*, 31,879–31,892, 1998.

Rosenfeld, D., and I. M. Lensky, Satellite-based insights into precipi-

tation formation processes in continental and maritime convective clouds, *Bull. Am. Meteorol. Soc*., *79*, 2457–2476, 1998.

Stephens, G. L., Radiation profiles in extended water clouds, I, Theory, *J. Atmos. Sci*., *35*, 2111–2122, 1978.

Stephens, G. L., *Remote Sensing of the Lower Atmosphere*, 523 pp., Oxford Univ. Press, New York, 1994.

Twomey, S., The nuclei of natural cloud formation, part II, The supersaturation in natural clouds and the variation of cloud droplet concentration, *Pure Appl. Geophys*., *43*, 243–249, 1959.

Twomey, S., Pollution and the planetary albedo, *Atmos. Environ*., *8*, 1251–1256, 1974.

Twomey, S., The influence of pollution on the short wave albedo of clouds, *J. Atmos. Sci*., *34*, 1149–1152, 1977.

Wetzel, M. A., and L. L. Stowe, Satellite-observed patterns in stratus cloud microphysics, aerosol optical thickness, and shortwave radiative forcing, *J. Geophys. Res*., *104*, 31,287–31,299, 1999.

G. Feingold, NOAA/ETL, 325 Broadway, Boulder, CO 80305, USA. (graham.feinfold@noaa.gov)

Y. J. Kaufman, J. Ramaprasad, and L. A. Remer, NASA Goddard Space Flight Center, Code 923, Greenbelt, MD 20777.

(Received August 1, 2000; revised December 18, 2000; accepted April 4, 2001.)